Optics Letters

Sum frequency generation from touching wires: a transformation optics approach

Shimon Elkabetz,* K. Nireekshan Reddy, and Y. Sivan

School of Electrical and Computer Engineering, Ben-Gurion, Be'er-Sheva 8410501, Israel
**Corresponding author: elshimon@post.bgu.ac.il*

Received 16 November 2020; revised 3 March 2021; accepted 22 March 2021; posted 23 March 2021 (Doc. ID 414940); published 21 April 2021

We employ transformation optics to study analytically nonlinear wave mixing from a singular geometry of touching plasmonic wires. We obtain the analytic solution of the near field and complement it with a solution of far-field properties. We find, somewhat surprisingly, that optimal efficiency (in both regimes) is obtained for the degenerate case of second-harmonic generation. We exploit the analytic solution obtained to trace this behavior to the spatial overlap of input fields near the geometric singularity. © 2021 Optical Society of America

https://doi.org/10.1364/OL.414940

Introduction. Second-order nonlinear optical wave interactions involve the coherent conversion of two input optical waves into a third wave whose frequency is the sum of that of the input waves [1]. This enables frequency conversion of optical waves, a phenomenon of both fundamental and practical importance [1].

As the strength of second-order optical nonlinear interactions is weak in most materials, efforts have been dedicated to finding ways to increase it. One of the promising ways to achieve this is the use of metal (plasmonic) nanostructures. The high local fields enabled by these structures can be of particular benefit for this purpose. Since most plasmonic materials are centrosymmetric, second-order nonlinear optical processes in metals are forbidden in the local bulk response [1], and thus are governed by surface symmetry-breaking effects [2–4].

Analytic solutions for the field distribution near plasmonic nanostructures are available for just the simplest structures. The complex second-order response makes such solutions even more rare for nonlinear wave interactions. Accordingly, the vast majority of analytic studies of nonlinear wave interactions in plasmonic nanostructures rely on numerical simulations.

Recently, we studied analytically surface second-harmonic generation (SHG) assisted by surface plasmon polaritons from nano metallic touching wires (TWs) surrounded by a transparent dielectric medium [5]. This structure is interesting because it is a singular plasmonic structure, known for its optimal ability to enhance the electromagnetic fields close to the touching point by several orders of magnitude [6,7]; they also provide an unusually wide spectral response. The unique analytic solution was enabled by the technique of conformal transformation optics (TO), which exploits the invariance of Maxwell's equations to coordinate transformations and the consequent preservation of material and spectral characteristics (Fig. 1). Similar to the linear case, we transformed to the simpler slab structure, solved, and then transformed back to the more complicated TW structure. This unique approach, one of the first ever to employ TO to nonlinear wave interactions, revealed rich physical insights. Specifically, our analysis demonstrated that apart from the mode-matching condition (see, e.g., [8]), the phase-matching condition is relevant even for this subwavelength structure. Furthermore, we identified a geometric factor that was not identified before and causes the field suppression close to the touching point [5]. In [9], we showed how to compute the scattering cross-section from the analytic solution obtained in [5] and performed an optimization of the SHG efficiency by tuning the background permittivity.

In this Letter, we attempt to further optimize the frequency conversion process by extending the analysis to (nondegenerate) three-wave mixing, in particular, to sum frequency generation (SFG). This provides one additional degree of freedom that is *a priori* expected to enable further improvement of the conversion efficiency as well as greater flexibility of the generated new frequency. To do that, we adapt the procedure presented in [5], and then analyze the final solution. Somewhat counterintuitively, we find that the degenerate case of SHG provides optimal conversion efficiency. Using the analytic solution, we are able to trace this behavior to nonlinear polarization, which is created by the overlap of the two incoming frequency waves. In particular, due to the rapidly oscillatory nature of the fields near the touching point, this overlap is found to be optimal for the degenerate case.

Configuration of Study. We are interested in the analytic solution for three-wave mixing from subwavelength TWs. Consider TM (x) polarized plane waves $E_{\mathrm{inc},x}^{\omega_{1,2}}$ at input frequencies $\omega_{1,2}$, which are incident perpendicularly upon a subwavelength pair of infinitely long touching metallic wires (Fig. 1). The sum frequency magnetic field $H_z^{\omega_3}$ is obtained by solving the Helmholtz equation under the quasistatic (QS) approximation ($\lim\ k_0 \to 0$) [5], namely,

$$\nabla \times \left[\nabla \times H_{z,\mathrm{TW}}^{\omega_3}(x,y)\hat{z}\right] = 0, \tag{1}$$

where x and y are the in-plane spatial coordinates. The boundary conditions for the electric and magnetic fields, to be applied on the metal–dielectric interfaces, are given by [10]

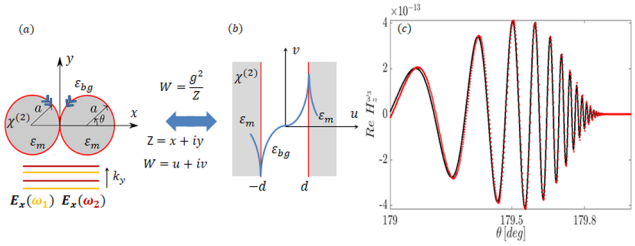

Fig. 1. (a) Touching wire dimer and (b) slab structure related through conformal inversion transformation. The incident plane waves $E_x^{\omega_{1,2}}$ are marked by red and yellow solid lines, $\chi^{(2)}$ is the second-order nonlinear surface tensor marked by red lines along the structures contours, $\varepsilon_{m/bg}$ are the permittivities of the metal/background, and $d=g^2/2a$ is the distance of the interfaces from the origin, where a is the wire radius and g^2 is a scaling constant. (c) Analytic (black solid line) and numeric (red dots) solutions of $H_{z,\mathrm{TW}}^{\omega_3}$ on the perimeter of the TWs as a function of the angle θ; $\omega_3=908$ THz, $\omega_1=375$ THz, and $\omega_2=533$ THz.

$$\mathbf{n}\times(\mathbf{H}_{bg}-\mathbf{H}_m)=H_{z,\mathrm{TW}}^{\omega_3}|_{bg}-H_{z,\mathrm{TW}}^{\omega_3}|_m=0, \tag{2}$$

$$E_{\parallel,\mathrm{TW}}^{\omega_3}|_{bg}-E_{\parallel,\mathrm{TW}}^{\omega_3}|_m=-\frac{1}{\varepsilon_{bg}}\nabla_\parallel P_{S,\perp}^{\omega_3}, \tag{3}$$

where $\mathbf{n}$ is the outward normal to the interface, and subscripts bg and m correspond to the dielectric and metal sides of the interface, respectively. The SFG frequency is given by $\omega_3=\omega_1+\omega_2$, and ε_{bg} is the background permittivity (assumed to be dispersionless). $P_{S,\perp}^{\omega_3}$ describes the normal to the surface component of the surface polarization vector, $\mathbf{P}_S^{(2)}$ [10].

For SFG, the nonlinear surface tensor $\chi_S^{(2)}$ contains three independent elements, the most dominant of which is $\chi_{S,\perp\perp\perp}^{(2)}$ [11]. This element describes perpendicular surface currents; therefore, the $P_{S,\perp}^{\omega_3}$ definition is given by

$$P_{S,\perp}^{\omega_3}=\chi_{S,\perp\perp\perp}^{(2)}E_{\perp,\mathrm{TW}}^{\omega_1}E_{\perp,\mathrm{TW}}^{\omega_2}\delta(x^2+y^2\mp 2ax), \tag{4}$$

where $E_{\perp,\mathrm{TW}}^{\omega_{1,2}}$ are the electric fields at the input frequencies $\omega_{1,2}$, perpendicular to the perimeter of TW geometry [6]. The source can be more conveniently written as a magnetic surface current density [12], given by

$$J_z=-\frac{1}{\varepsilon_{bg}}\nabla_\parallel P_{S,\perp}^{\omega_3}. \tag{5}$$

The boundary condition for the electric field, Eq. (3), in terms of the magnetic field, is given by

$$\left(\frac{x\pm a}{a}\right)\left[\frac{1}{\varepsilon_{bg}}\frac{\partial H_{z,\mathrm{TW}}^{\omega_3}}{\partial x}|_{bg}-\frac{1}{\varepsilon_m^{\omega_3}}\frac{\partial H_{z,\mathrm{TW}}^{\omega_3}}{\partial x}|_m\right]+\frac{y}{a}\left[\frac{1}{\varepsilon_{bg}}\frac{\partial H_{z,\mathrm{TW}}^{\omega_3}}{\partial y}|_{bg}-\frac{1}{\varepsilon_m^{\omega_3}}\frac{\partial H_{z,\mathrm{TW}}^{\omega_3}}{\partial y}|_m\right]=i\frac{\omega_3\varepsilon_0}{\varepsilon_{bg}}\nabla_\parallel P_{S,\perp}^{\omega_3}, \tag{6}$$

where ε_0 is the vacuum permittivity, and $\varepsilon_m^{\omega_3}$ is the metal permittivity at ω_3.

According to [6], under the QS approximation, the linear electric response fields, $\mathbf{E}^{\omega_{1,2}}$, which appear in Eq. (4), can be derived by differentiating the electric potential $\phi^{\omega_{1,2}}$. Specifically,

$$\mathbf{E}^{\omega_{1,2}}=\nabla_{x,y}\phi^{\omega_{1,2}}, \tag{7}$$

$$\phi^{\omega_{1,2}}=-\left(\frac{a\pi\varepsilon_{bg}}{\varepsilon_m^{\omega_{1,2}}+\varepsilon_{bg}}\right)\exp\left(\frac{-\alpha^{\omega_{1,2}}ax}{x^2+y^2}\right)\exp\left(\frac{i\alpha^{\omega_{1,2}}a|y|}{x^2+y^2}\right), \tag{8}$$

where a is the radius of a single wire, $\varepsilon_m^{\omega_{1,2}}$ are the metal permittivities at the input frequencies, and $\alpha^{\omega_{1,2}}$ are the corresponding dimensionless propagation constants, given by

$$\alpha^{\omega_{1,2}}=\ln\left(\frac{\varepsilon_m^{\omega_{1,2}}-\varepsilon_{bg}}{\varepsilon_m^{\omega_{1,2}}+\varepsilon_{bg}}\right),\quad \mathrm{Re}[\varepsilon_m^{\omega_{1,2}}]<-\varepsilon_{bg}. \tag{9}$$

We note that the form of Eq. (9) is just the dispersion relation of SPPs in a metal–dielectric–metal structure under QS approximation.

Using Eq. (8), the magnetic surface current in the TW frame (4) can be rewritten as

$$J_{z,r/l}(x,y)=\frac{\chi_{S,\perp\perp\perp}^{(2)}}{\varepsilon_{bg}}\partial_\parallel(E_{\perp,\mathrm{TW}}^{\omega_1}E_{\perp,\mathrm{TW}}^{\omega_2})\delta(x^2+y^2\mp 2ax), \tag{10}$$

where $J_{z,r}$ and $J_{z,l}$ are the magnetic current densities on the right and left wires, respectively. Since the parallel derivative does not change the complex exponential function, the magnetic surface currents can be decomposed as

$$J_{z,r}(x,y)=\mathcal{R}(x,y)\exp\left(\frac{i\alpha_s a|y|}{x^2+y^2}\right)\delta(x^2+y^2-2ax), \tag{11}$$

$$J_{z,l}(x,y)=\mathcal{L}(x,y)\exp\left(\frac{i\alpha_s a|y|}{x^2+y^2}\right)\delta(x^2+y^2+2ax). \tag{12}$$

The input electric fields [see Eq. (8)] are symmetric in x and y, so that their product is symmetric as well. According to Eq. (10), the parallel derivative changes this symmetry, and therefore, $J_{z,r}(x,y)$ is anti-symmetric in x and y, i.e., $J_{z,r}(x,y)=-J_{z,l}(-x,y)$ and $J_{z,r}(x,y)=-J_{z,l}(x,-y)$ (see [5,9]). As shown in [9], this yields a quadrupolar field pattern. For simplicity, from now on, we can refer only to the right wire.

Analytical Solution in the Slab Frame. We now apply the TO procedure used previously in [5] to study SFG. Specifically, since $H_z^{\omega_3}$ is preserved under the conformal inversion transformation [5], we can simplify the TWs problem by using conformal inversion transformation to transform from the touching dimer frame to a slab frame, solve the resulting (simpler) equations, and transform back (Fig. 1).

First, we employ the inversion conformal transformation, given by

$$x=\frac{g^2u}{u^2+v^2},\quad y=\frac{g^2v}{u^2+v^2}, \tag{13}$$

$$u=\frac{g^2x}{x^2+y^2},\quad v=\frac{g^2y}{x^2+y^2}, \tag{14}$$

where g^2 is a scaling constant, and u and v are the transformed frame coordinates. Hence, after injecting Eq. (5) and Eqs. (11) and (12), the boundary conditions (3) take the form

$$\left(\frac{v^2+d^2}{g^2}\right)\partial_u\left[\frac{H^{\omega_3}_{z,sl}|_{bg}}{\varepsilon_{bg}}-\frac{H^{\omega_3}_{z,sl}|_{m}}{\varepsilon^{\omega_3}_{m}}\right]$$

$$=\pm i\omega_3\varepsilon_0\Delta_{r/l}(u=\pm d,\,v)e^{-i\alpha_s|v|/d},\quad u=\pm d, \tag{15}$$

where d is the distance from the interface to the origin (Fig. 1), and $\Delta_{r,l}(u,\,v)$ are defined as

$$\Delta_r(u,\,v)\equiv\mathcal{R}\left(\frac{g^2u}{u^2+v^2},\frac{g^2v}{u^2+v^2}\right), \tag{16}$$

$$\Delta_l(u,\,v)\equiv\mathcal{L}\left(\frac{g^2u}{u^2+v^2},\frac{g^2v}{u^2+v^2}\right). \tag{17}$$

According to the anti-symmetry of the magnetic surface currents, $\mathcal{R}(x,\,y)$ and $\mathcal{L}(x,\,y)$ are anti-symmetric as well; hence, the boundary conditions (15) are identical.

To calculate the fields on the boundaries, we adopt the slowly varying amplitude approximation and define an ansatz solution, similar to [5], based on the following considerations:

- Since we expect surface plasmon waves to occur, the solution must have exponential decay (along the transverse coordinate u), while the longitudinal dependence (along v) has to be oscillatory.
- The anti-symmetric source [magnetic current density (10)] dictates an anti-symmetric solution.
- The propagation constant of the solution (i.e., the y dependence) has to be the same as that of the source α_s, defined as

$$\alpha_s=\frac{\alpha^{\omega_1}+\alpha^{\omega_2}}{2}. \tag{18}$$

Accordingly, the ansatz solution will be

$$H^{\omega_3}_{z,sl}=\frac{-i\omega_3\varepsilon_0g^2d}{\alpha_s\mathcal{P}}\left(\frac{\Delta_r(u=d,\,v)}{v^2+d^2}\right)e^{i\alpha_s|v|/d}$$

$$\times\begin{cases}\sinh(\alpha_s u/d), & |u|<d,\\ \mathrm{sgn}[u]\sinh(\alpha_s)e^{\alpha_s(1-|u|/d)}, & |u|>d,\end{cases} \tag{19}$$

where $\mathcal{P}$ is the so-called phase-matching (PM) factor, given by [5]

$$\mathcal{P}=\cosh(\alpha_s)+\frac{\varepsilon_{bg}}{\varepsilon^{\omega_3}_{m}}\sinh(\alpha_s).$$

Analytical Solution in the TW Frame. As mentioned above, $H^{\omega_3}_{z,sl}$ is preserved under inverse conformal transformation back to the TW frame; thus, we can now find the solution in the touching dimer simply by transforming back into that frame. This gives

$$H^{\omega_3}_{z,\mathrm{TW}}(x,\,y)=\frac{-4i\omega_3\varepsilon_0a}{\alpha_s\mathcal{P}}\left(\frac{r^4\mathcal{R}(\tau_x,\,\tau_x)}{4a^2y^2+r^4}\right)e^{i2a\alpha_s|y|/r^2}$$

$$\times\begin{cases}\sinh(2a\alpha_s x/r^2), & r^2+2a|x|>0,\\ \mathrm{sgn}[x]\sinh\alpha_s\,e^{\alpha_s(1-2a|x|/r^2)}, & r^2+2a|x|<0,\end{cases} \tag{20}$$

where $r^2=x^2+y^2$, such that $r^2+2a|x|>0\,(<0)$ correspond to regions outside (inside) the TWs, and τ_x and τ_y are coordinates defined as

$$(\tau_x,\,\tau_y)=\left(\frac{1/(2a)}{1/(4a^2)+y^2/(x^2+y^2)^2},\right.$$

$$\left.\frac{y/(x^2+y^2)}{1/(4a^2)+y^2/(x^2+y^2)^2}\right). \tag{21}$$

These coordinates map points in the domain outside the TWs to the TWs' perimeter [9]. Since $H^{\omega_3}_{z,\mathrm{TW}}$ is continuous in the entire space, it would be interesting to find the spatial variation of $H^{\omega_3}_{z,\mathrm{TW}}$ on the perimeter of the wires close to the touching point. This arc obeys $x^2+y^2=2ax$, so that

$$H^{\omega_3}_{z,\mathrm{TW}}(x,\,y)=-i\omega\varepsilon_0\left[\frac{\sinh\alpha_s}{\alpha_s\mathcal{P}}\right]x\mathcal{R}(x,\,y)\exp\left(\frac{2ia\alpha_s y}{x^2+y^2}\right). \tag{22}$$

Using Eq. (11), this equation can be rewritten as

$$H^{\omega_3}_{z,\mathrm{TW}}(x,\,y)=-i\omega\varepsilon_0\varepsilon_{bg}\left[\frac{\sinh\alpha_s}{\alpha_s\mathcal{P}}\right]xJ_{z,r}(x,\,y). \tag{23}$$

This is the generalization of the solution presented in [5] to the (nondegenerate) case of SFG.

As previously in [5], we support the analytic result (23) with numeric simulations based on the finite element method using the commercially available package COMSOL Multiphysics (V 3.5a) (see discussion in Appendix E, [5]). We again observe excellent agreement [Fig. 1(c)].

Discussion. Having obtained the solution for SFG, we can now find the conditions for optimal efficiency. To do that, we first calculate the maximum magnetic (near) field, $\max|H^{\omega_3}_z|$, on the perimeter of the right wire for all $\omega_{1,2}$ combinations in the range of 200–900 THz that yields a fixed value of ω_3. We find that the strongest response is obtained in the degenerate case (SHG), i.e., when $\omega_1=\omega_2$ [Fig. 2(a)]. We can also go beyond the near-field calculation of [5] and investigate whether the far-field calculations exhibit the same SHG superiority as the near fields. To do that, using the recipe described in [9], we compute analytically and numerically the expressions for the scattering cross-section of the TWs for the SFG case, $\sigma^{\omega_3}_{\mathrm{scat}}$. Specifically, we calculate the scattered power (on the contour $\mathcal{S}$ enclosing the TWs):

$$P^{\omega_3}_{\mathrm{scat}}=\frac{1}{2}\int_{\mathcal{S}}\mathrm{Re}(E^{\omega_3}_{\phi}[H^{\omega_3}_z]^*)\mathrm{d}\mathcal{S}, \tag{24}$$

where $E^{\omega_3}_{\phi}$ represents the parallel component of the SFG electric field along the contour $\mathcal{S}$. The SFG frequency is fixed for different values of $\omega_3=850$ and 670 THz. In Fig. 2(c), we observe an excellent agreement between analytic and numeric solutions for the cross-sections. Furthermore, we also observe the superiority of the SHG in the far-field study. This result is consistent with the conclusion drawn in [9] that $J_{z,r}$ is the dominant element determining the far-field response.

This somewhat unexpected result is the main one of this work.

To understand why the SHG is superior over all other SFG combinations, we analyze the elements of the solution (23) in Fig. 2(b). On one hand, we observe that the amplitude

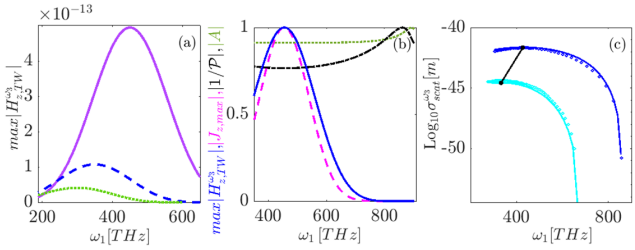

Fig. 2. (a) Analytic solution of max $|H_z^{\omega_3}|$ for $\omega_3 = 900$ THz (solid purple line), 700 THz (dashed blue line), and 600 THz (dotted green line). The degenerate cases, $\omega_1 = 450$, 350, 300 THz, are marked by dashed lines. (b) Comparison of the elements (normalized absolute value) of the analytic solution, Eq. (23), at $\omega_3 = 909$ THz. A (dotted green line) represents amplitude, $1/\mathcal{P}$ represents the phase-matching element (dashed-dotted black line), $\max(H_z)$ is the maximum SFG magnetic field (solid blue line), and $\max(J_z)$ (dashed magenta line) is the maximum magnetic current. (c) Analytic (line) and numeric (dots) scattering cross-section. Two plots for fixed SFG frequencies $\omega_3 = 850$ and 670 THz, represented by the blue and cyan lines, respectively. The black line represents the trajectory of the SHG combinations.

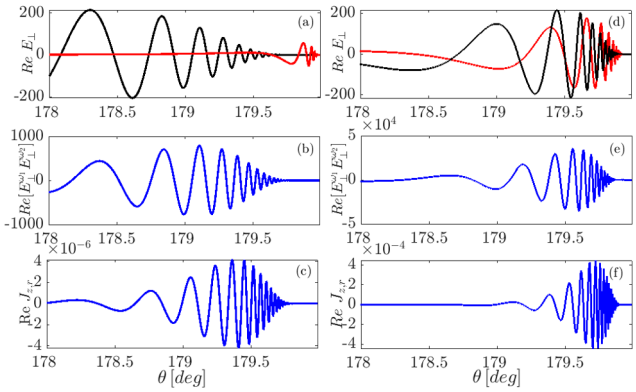

Fig. 3. (a) Re$[E_\perp]$ for $\omega_1 = 200$ THz (red solid line) and $\omega_2 = 708$ THz (black solid line), (b) Re$[E_\perp^{\omega_1} E_\perp^{\omega_2}]$, and (c) Re$[J_{z,r}]$. (d)–(f) Same as (a)–(c) for a smaller frequency difference, namely, $\omega_1 = 408$ THz (red solid line) and $\omega_2 = 500$ THz (black solid line).

$A = -i\omega\varepsilon_0\varepsilon_{bg}\sinh\alpha_s/\alpha_s$ and the PM factor are nearly independent of frequency, at least in the regime where the SFG is maximal. On the other hand, we observe a similar trend for $\max|H_{z,\mathrm{TW}}^{\omega_3}|$ and for the maximum absolute magnetic current density, $\max|J_{z,r}|$. Therefore, we conclude that $J_{z,r}$ has the dominant effect on $H_{z,\mathrm{TW}}^{\omega_3}$.

Thus, we look more carefully at the constituents of the source term $J_{z,r}$. Equation (11) shows that like in any three-optical-wave nonlinear interaction, the source is proportional to the product of the incident fields. The highly oscillatory nature of these fields close to the touching point means necessarily that optimal overlap is obtained when the frequencies of the incident plane waves are identical. Otherwise, the overlap (and hence, the overall amplitude of the source) deteriorates with the frequency difference (Fig. 3). Thus, unlike the prior expectation that the additional degree of freedom enabled by SFG compared with SHG will yield better efficiency, we find that SHG is optimal for the near fields of the TWs.

Conclusion. We have shown that the additional degree of freedom obtained by allowing the incoming frequencies to differ does not provide additional improvement in the efficiency of the frequency conversion process. Our analysis shows that this originates from the highly oscillatory nature of the fields near the touching point. A similar conclusion is thus expected also for difference frequency generation [13] or four-wave mixing in such structures. Conversely, nearly degenerate difference frequency generation (in particular, terahertz emission; see, e.g., [14,15]) is thus expected to be efficient.

The analysis described in this work could be easily extended to the study of additional problems in nonlinear optics using TO, such as the study of non-local nonlinear effects (using, e.g., the formulations in [16,17]), as well as the study of other structures such as non-TWs or other singular structures [18], 3D particle configurations [19], and (singular) gratings and 2D materials [7].

Funding. Israel Science Foundation (899/16).

Disclosures. The authors declare no conflicts of interest.

Data Availability. Data underlying the results presented in this paper are not publicly available at this time but may be obtained from the authors upon reasonable request.

REFERENCES

1. R. W. Boyd, *Nonlinear Optics*, 2nd ed. (Academic, 2003).
2. N. Bloembergen, R. Chang, S. Jha, and C. Lee, Phys. Rev. **174**, 813 (1968).
3. J. Rudnick and E. Stern, Phys. Rev. B **4**, 4274 (1971).
4. J. E. Sipe, V. So, M. Fukui, and G. Stegeman, Phys. Rev. B **21**, 4389 (1980).
5. K. N. Reddy, P. Y. Chen, A. I. Fernández-Domínguez, and Y. Sivan, Phys. Rev. B **99**, 235429 (2019).
6. D. Y. Lei, A. Aubry, and S. A. Maier, New J. Phys. **12**, 093030 (2010).
7. F. Yang, P. A. Huidobro, J. B. Pendry, and P. F. Brevet, Phys. Rev. B **98**, 125409 (2018).
8. J. B. Khurgin and G. Sun, Opt. Express **20**, 28717 (2012).
9. S. Elkabetz, K. N. Reddy, P. Y. Chen, A. I. Fernández-Domínguez, and Y. Sivan, Phys. Rev. B **103**, 075411 (2021).
10. K. N. Reddy, P. Y. Chen, A. I. Fernández-Domínguez, and Y. Sivan, J. Opt. Soc. Am. B **34**, 1824 (2017).
11. G. B. J. Butet, I. Russier-Antoine, C. Jonin, E. Benichou, and P. F. Brevet, Phys. Rev. B **82**, 235403 (2010).
12. M. K. J. Maitalo and S. Suuriniemi, Opt. Express **19**, 23386 (2011).
13. F. Che, S. A. Ponomarenko, and M. Cad, J. Opt. **18**, 125503 (2016).
14. Z. Ruan, G. Veronis, K. Vodopyanov, M. Fejer, and S. Fan, Opt. Express **17**, 13502 (2009).
15. E. Minerbi, S. Keren-Zur, and T. Ellenbogen, Nano Lett. **19**, 6072 (2019).
16. A. I. Fernández-Domímguez, P. Zhang, Y. Luo, S. A. Maier, F. J. Garcia-Vidal, and J. B. Pendry, Phys. Rev. B **86**, 241110 (2012).
17. A. I. Fernández-Domímguez, A. Wiener, F. J. Garcia-Vidal, S. A. Maier, and J. B. Pendry, Phys. Rev. Lett. **108**, 106802 (2012).
18. Y. Luo, J. Pendry, and A. Aubry, Nano Lett. **10**, 4186 (2010).
19. A. I. Fernández-Domímguez, Y. Luo, A. Wiener, J. B. Pendry, and S. A. Maier, Nano Lett. **12**, 5946 (2012).

132.73.208.180 on 2021-04-21 07:19:07